



TITLE:

Seismic recordings of landslides caused by Typhoon Talas (2011), Japan

AUTHOR(S):

Yamada, Masumi; Matsushi, Yuki; Chigira, Masahiro; Mori, Jim

CITATION:

Yamada, Masumi ...[et al]. Seismic recordings of landslides caused by Typhoon Talas (2011), Japan. Geophysical Research Letters 2012, 39(13): L13301.

ISSUE DATE:

2012-07-07

URL:

<http://hdl.handle.net/2433/159904>

RIGHT:

©2012. American Geophysical Union.; This is not the published version. Please cite only the published version.; この論文は出版社版ではありません。引用の際には出版社版をご確認ご利用ください。

Seismic Recordings of Landslides Caused by Typhoon Talas (2011), Japan

Authors

*Masumi Yamada¹

Yuki Matsushi^{1,2}

Masahiro Chigira¹

Jim Mori¹

Affiliations

1 Disaster Prevention Research Institute, Kyoto University

Gokasho, Uji, Kyoto, 611-0011, Japan

M.Y., Y.M., J.M., and M.C.

2 CREST, Japan Science and Technology Agency

K's Gobancho, 7, Gobancho, Chiyoda-ku, Tokyo, 102-0076 Japan

Y.M.

Corresponding author

Correspondence to: Masumi Yamada

Large deep-seated landslides occurred in Nara, Wakayama, and Mie prefectures of western Japan when Typhoon Talas passed through the region on September 3-4, 2011. Signals of large landslides have been recorded by seismic networks around the world, and overall force estimates have been previously determined for large landslides using long-period waves. This study focuses on the high-frequency waveforms and presents signals of 18 landslides caused by Typhoon Talas (2011). The location of the landslides can be determined by a seismological back-projection technique and these locations correlate with the observed surface features. We have found that the volumes of the landslide correlated with an energy parameter derived from the seismic records.

1. Introduction

When Typhoon Talas moved through western Japan on September 3-4, 2011, there were extensive slope failures across a wide region in Nara, Wakayama, and Mie prefectures. Heavy rainfall, exceeding 2000 mm on the Kii peninsula, triggered these destructive landslides which killed 97 people [*Fire and disaster Management Agency*, 2011]. Previously, signals of large landslides have been recorded by seismic networks around world [e.g. *Kanamori et al.*, 1984; *La Rocca et al.*, 2004; *Surinach et al.*, 2005; *Tang et al.*, 2009; *Favreau et al.*, 2010; *Lin et al.*, 2010; *Feng*, 2011 ; *Hibert, et al.*, 2011] and the long-period data are useful for determining the force-history of landslides. A force generated by the mass sliding can be inverted by matching the phase and amplitudes of the observed data to theoretical waveforms [e.g. *Kanamori et al.*, 1984; *Brodsky et al.*, 2003; *Stark and Ekstrom* 2010]. Here we focus on the more complicated high-frequency waveforms recorded by high-sensitivity networks. The station distribution is much denser than for broadband stations in Japan, so that analytical results of the data can have higher resolution in time and space [*Ohsumi et al.*, 2005; *Ohsumi et al.*, 2006]. This study presents signals of 18 landslides caused by Typhoon Talas (2011), which were detected by high-frequency waveforms. These landslides can be located by a back-projection technique, and the volumes of the landslides correlate with an energy parameter determined from the seismic records.

2. Data

The seismic signals due to these landslides were recorded by dense seismic networks in Japan. The low-frequency surface waves of the larger landslides were recorded across all of Japan by the broadband seismic network F-net [*National Research Institute for*

Earth Science and Disaster Prevention, 2010]. Higher frequency waves were also recorded by high-gain seismic networks (Hi-net, Japan Meteorological Agency, and university networks) at distances up to a few hundred kilometers. The landslide signals are usually tens of seconds in duration and show emergent onsets, thus they can be easily distinguished from records of small earthquakes, which have different shapes and shorter duration.

Figure 1(a) shows the Akatani landslide signal recorded by a broadband seismometer 35 km away from the source. Filtering of the data shows that the high-frequency (>1 Hz) and low-frequency (<0.1 Hz) components of the waveform have different characteristics. The onset of the large amplitude low-frequency motion is about 20 sec earlier than the initiation of the observable high-frequency motions. The low-frequency component shows the peak amplitude significantly earlier than the peak amplitudes of the high-frequency component.

The low-frequency component can be modeled assuming a single force for a mass sliding down the slope. The size of the maximum force generated by the mass sliding was estimated as 7×10^{10} N with a total duration of 70 sec, using modeling of broadband waveforms from 18 regional stations in Japan [*National Research Institute for Earth Science and Disaster Prevention*, 2011]. The low-frequency component reflects the progressive unloading and reloading of the solid earth beneath the slide, while much of the high-frequency component probably is generated by complicated multiple momentum exchanges between landslide debris clasts and the bed as it is sliding. The earlier onset of the long-period waves suggests that the landslide starting sliding rather smoothly as a coherent block. The large amplitude in the high-frequency waveform at about 150 sec may be related to a fairly sudden stopping of part of the landslide. From field observations it can be seen that the Akatani event was stopped when it hit the opposite valley wall (see Figure 1(b)).

The landslide sequence was distributed over a broad area, so data from the dense high-gain short-period networks (about 20 km spacing) were used for the analyses. Applying a 4th order Butterworth band-pass filter (1-4 Hz) to the seismograms recorded between September 3rd and 5th, we identified 18 landslide events (see Table 1) which are seen on multiple stations.

3. Back-projection Analysis

In order to determine the location and timing of the landslide, we applied a back-projection technique [*Spudich and Cranswick*, 1984] to the seismic records. The advantage of the back-projection is that little prior information is necessary and the

results are reasonably stable. We process the seismic data with the following procedure.

1. An envelope of the band-passed records is calculated using a Hilbert transform.
2. A mean smoothing algorithm with a window of 200 samples (2 seconds) is applied.
3. The noise amplitude is subtracted from the data.
4. The maximum amplitude is normalized to a value of 1.0. This process reduces the effect of high-frequency noise and makes the results of back-projection more stable.

We use the Japan Meteorological Agency 1-D velocity structure, and assume an S-wave velocity for the analysis. The recorded waves are likely a mixture of S and surface waves with a velocity close to the S-wave velocity. First, we perform the back-projection with all the available data. Then, the location is refined in a second iteration by repeating the process using only the near-source data corresponding to the most probable location determined in the first iteration. The probability distribution for the location of the second iteration for the 09040722 event is shown in Figure 2. There are several landslides very close to the most probable location of this signal. However, this event shows significantly large amplitudes in the seismic records, so we inferred that this signal is from the Akatani landslide, which has the largest volume of sliding mass among the possible sources. The band-passed waveforms and envelopes of the Akatani landslide are shown in Figure 3. The timing is aligned and the amplitude decays as a function of distance, which shows qualitatively that the location is reasonable. We also used information provided by local witnesses and personal communications with electric power companies when there were multiple choices for an event (See Supporting Table 1 and Supporting Figure 2). We located 13 events out of 18 by this method, and the other 5 events have multiple solutions so the location is not well resolved.

The largest landslide was the Kuridaira event, with a total volume of 13.6 million m³. The main collapse of the Kuridaira event occurred at 23:06 on September 3 followed by subsequent minor slides (See Supporting Figure 1). A second slide occurred at 23:07, and third at 23:12. Since waves from a distant M7 earthquake arrived at about the same time as the occurrence of the landslide, the onsets of the landslide records are contaminated by the teleseismic P-waves. However, main energy of the landslide can be separable from the earthquake, since the largest amplitudes from the landslide are about 20 seconds after the onset of the teleseismic P-wave arrival.

4. Size Estimate of Landslides

In order to quantify the size of the seismic signals, we use the sum of the squared band-passed velocity data as an energy parameter. Note that with a distance correction, this measurement is proportional to the radiated seismic energy [Kanamori *et al.*, 1993;

Suwa et al., 2003] in this frequency range. Since we are using band-pass filtered records, it is not equal to the total radiated energy of the landslide movement. Here we simply use the sum of the squared velocity and define it as our energy parameter,

$$\text{Energy parameter } E = \sum_{t=t_0}^{t=t_1} v(t)^2 dt \quad (1)$$

where $v(t)$ is the 1-4Hz band-pass filtered velocity record (cm/s) at time t , t_0 is a trigger time when the standard deviation of a 10 s record exceeds twice the amplitude of the noise level, t_1 is a threshold time when the standard deviation becomes smaller than 1.5 times of the noise level, and dt is the sampling interval of 0.01 s. Integration over time takes into account the duration of the signal as well as the amplitude. Since amplitudes of the signals can be significantly affected by the subsurface soil amplification, we use data recorded at only the borehole sites. The source-station distance range is 1 to 80 km for this analysis. From these data it is difficult to discuss the physical interpretation of this band-limited energy estimate, because we do not know the shape of the source spectrum across a wide frequency range.

Figure 4(a) shows the relationship between the source-station distance and this measurement. The energy parameter shows larger amplitude for large landslides (e.g. Kuridaira, Akatani) and decays as a function of distance. However, the slope seems to be similar for all events. Using these data, we can empirically derive an attenuation relation. Therefore, we regress the dataset using a linear function with a constant slope α and determine the intercept β_i for each event i .

$$\log_{10} E = \alpha \log_{10} R + \beta_i \quad (2)$$

where R is the source-station distance (km). The optimal slope minimizing the error for 11 landslides is -2.15, and the value of β_i for each event is shown in Table 1. The Kuridara event was not used in the regression because it is contaminated by a distant earthquake. The β_i value for the Kuridaira events was later evaluated using the optimal value of α from the regression.

The values of β_i represent the log of the high-frequency radiated energy at a distance of 1 km from the source. Since we have the locations of the landslides, we can correlate the seismic signals with the observed surface features. We compared the high-frequency energy values with the volumes of the landslides, as estimated from airborne LiDAR (light detection and ranging) topographic surveys before and after the

event, where available. Otherwise the volume is estimated from 5 or 10 m-mesh digital elevation models and aerial photographs. Although there is a fairly large variation for the small events, in general, there appears to be a good correlation of the energy parameter with the landslide volume (Figure 4(b)). If a linear relation is fit to the data, the regression equation is expressed as;

$$E|_{R=1km} = 8.5 \times 10^{-20} V^{2.06} \quad (3)$$

where V is the volume of the landslides. Note that this equation shows the band-limited energy parameter is approximately correlated with the square of the volume of the landslides. Physically, this energy parameter may be related to the mass (and maybe some unknown quantity) of the landslides, or alternatively this high-frequency energy may be more related to the dynamic properties of the moving slide. Using this empirical relationship the energy parameter of the seismic records can be used to determine the size of remotely detected landslides.

5. Conclusions

The landslides caused by Typhoon Talas (2011) represent one of the best recorded sequences of catastrophic deep-seated landslides in the world. The events can be located by conventional seismological techniques, and the volumes of the landslide correlated with the energy parameter of the seismic records. The seismic signals can provide information about the energy radiation and durations of the landslides, which are rarely obtained from visual observations [Suwa *et al.*, 2010; Socio *et al.*, 2008]. Although the seismic networks were originally designed for locating earthquakes, the continuously recorded data can be very important for understanding the mechanisms of other natural phenomenon, such as landslides. These high sensitivity networks are part of the earthquake early warning system and data are transferred in real time. Therefore, using the techniques shown here, there is a possibility to determine the locations and sizes of landslides within a minute of their occurrences. Such information can be useful for prompt emergency information, rescue efforts, and mitigation of further damage from these large landslides.

Acknowledgements

We acknowledge the National Research Institute for Earth Science and Disaster Prevention (NIED), Japan Meteorological Agency (JMA), and Japanese universities for

the use of the seismic data. High-resolution DEM data, which have been used to calculate landslide volumes, were provided by the Nara Prefectural Government and the Kinki Regional Development Bureau, Ministry of Land, Infrastructure and Transport. We thank Dr. Colin Stark and an anonymous reviewer for their helpful comments.

References

- Brodsky, E., E. Gordeev, and H. Kanamori (2003), Landslide basal friction as measured by seismic waves, *Geophysical Research Letters*, **30**, doi:10.1029/2003GL018485.
- Favreau, P., A. Mangeney, A. Lucas, G. Crosta, and F. Bouchut (2010), Numerical modeling of landquakes. *Geophysical Research Letters* **37**, L15305.
- Feng, Z. (2011), The seismic signatures of the 2009 Shiaolin landslide in Taiwan, *Nat. Hazards Earth Syst. Sci.* **11**, 1559–1569.
- Fire and Disaster Management Agency (2011), Report of the Disasters in 2011 <http://www.fdma.go.jp/bn/2012> (April 23, 2012, last accessed).
- Hibert, C., A. Mangeney, G. Grandjean, and N. Shapiro (2011), Slope instabilities in Dolomieu crater, Reunion Island: From seismic signals to rockfall characteristics. *Journal of Geophysical Research* **116**, F04032, doi:10.1029/2011JF002038.
- Kanamori, H., J. Mori, E. Hauksson, T.H. Heaton, L.K. Hutton, and L.M. Jones (1993), Determination of earthquake energy release and ML using TERRAScope. *Bulletin of the Seismological Society of America* **83**(2), 330–346.
- Kanamori, H., J. W. Given, and T. Lay (1984), Analysis of seismic body waves excited by the Mount St. Helens eruption of May 18, 1980, *J. Geophys. Res.* **89**, 1856–1866.
- La Rocca, M., D. Galluzzo, G. Saccorotti, S. Tinti, G.B. Cimini, and E. Del Pezzo (2004), Seismic signals associated with landslides and with a tsunami at Stromboli volcano, Italy. *Bulletin of the Seismological Society of America* **94**(5), 1850–1867.
- Lin, C.H., H. Kumagai, M. Ando, and T.C. Shin (2010), Detection of landslides and submarine slumps using broadband seismic networks. *Geophysical Research Letters* **37**(5), doi:10.1029/2010GL044685.
- National Research Institute for Earth Science and Disaster Prevention (2011), Observation of the seismic signals from the landslides due to Typhoon No.12. http://www.bosai.go.jp/press/2011/pdf/20110912_02.pdf (April 23, 2012, last accessed).
- Sosio, R., G.B. Crosta, and O. Hungr (2008), Complete dynamic modeling calibration for the Thurwieser rock avalanche (Italian Central Alps). *Engineering Geology* **100**(1-2), 11–26.
- Osumi, T., H. Asahara, E. Shimokawa (2005), Analysis of Ground-vibration induced by

the 10 August 2004, Ohtou Landslide in Nara Prefecture, Japan using the Data of High Sensitivity Seismograph Network : Application to Landslide Detecting, *Journal of Japan Society for Natural Disaster Science*, **24(3)**, 267-277 (in Japanese).

Osumi, T., H. Asahara, E. Shimokawa (2006), Hypocenter Detecting Analysis using the Data of High Sensitivity Seismograph Network applied for the Mass Movement on Mt. Shirouma, Nagano in 2005, *Journal of the Japan Landslide Society : landslides*, **43(1)**, 27-32 (in Japanese).

Spudich, P. and E. Cranswick (1984), Direct observation of rupture propagation during the 1979 Imperial Valley earthquake using a short baseline accelerometer array. *Bulletin of the Seismological Society of America* **74(6)**, 2083-2114.

Stark, C. and G. Ekstrom (2010), Landslide Force History inversion: Measuring the dynamics of catastrophic landslides using seismology and satellite remote-sensing, 2nd GIS- Landslide Meeting, Kyoto University, Nov. 2010.

Surinach, E., I. Vilajosana, G. Khazaradze, B. Biescas, G. Furdada, and J.M. Vilaplana (2005), Seismic detection and characterization of landslides and other mass movements. *Natural Hazards and Earth System Science* **5**, 791-798.

Suwa, H., J. Akamatsu, and Y. Nagai (2003), Energy radiation by elastic waves from debris flows. *Proceedings of the Third International Conference on Debris-Flow Hazards Mitigation*, 895-904.

Suwa, H., T. Mizuno, and T. Ishii, (2010), Prediction of a landslide and analysis of slide motion with reference to the 2004 Ohto slide in Nara. *Japan, Geomorphology* **124(3-4)**, 157-163.

Tang, C.L., J.C. Hu, M.L. Lin, J. Angelier, C.Y. Lu, Y.C. Chan, and H.T. Chu (2009), The Tsaoling landslide triggered by the Chi-Chi earthquake, Taiwan: Insights from a discrete element simulation. *Engineering Geology* **106(1-2)**, 1-19.

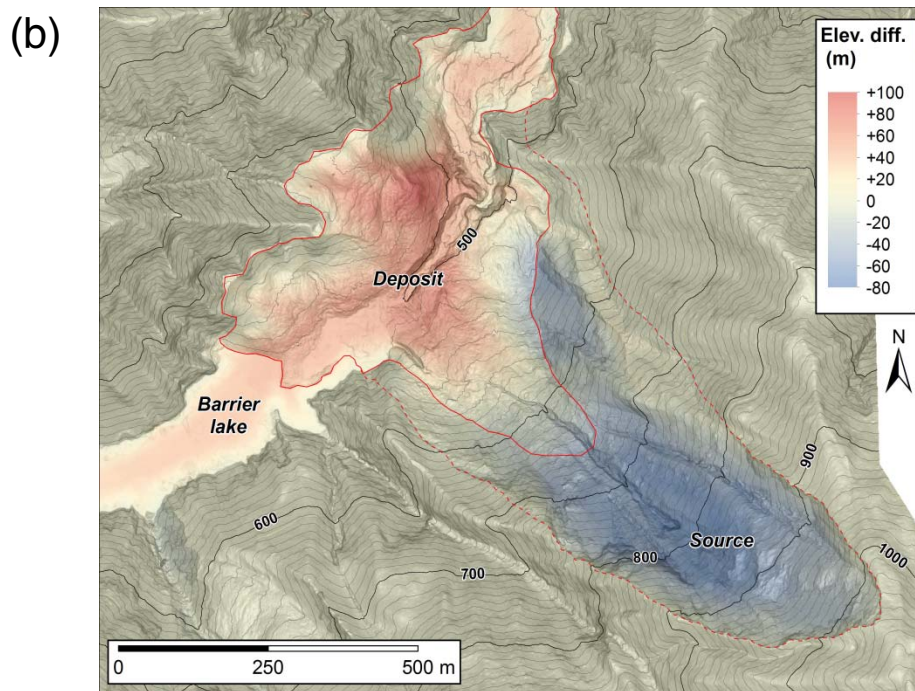
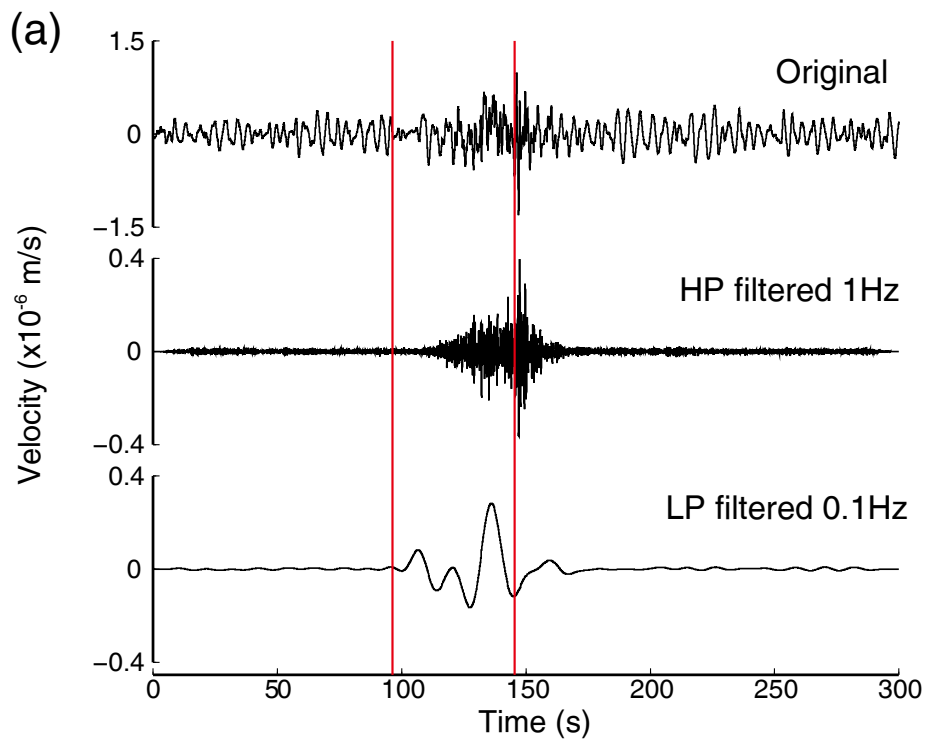


Fig. 1 (a) Broadband seismic records of Akatani landslide at NOKF station. The vertical lines show the onset and approximate time of impact on the far valley wall. Original record, high-pass filtered record at 1Hz, low-pass filtered record at 0.1Hz from the top.

(b) Elevation change at the Akatani landslide estimated from airborne LiDAR topographic surveys. The projected coordinate system is the Japan plane rectangular coordinate system zone 6, and the location of the landslide center is 34.126°N and 135.725°E in the WGS84 coordinate system.

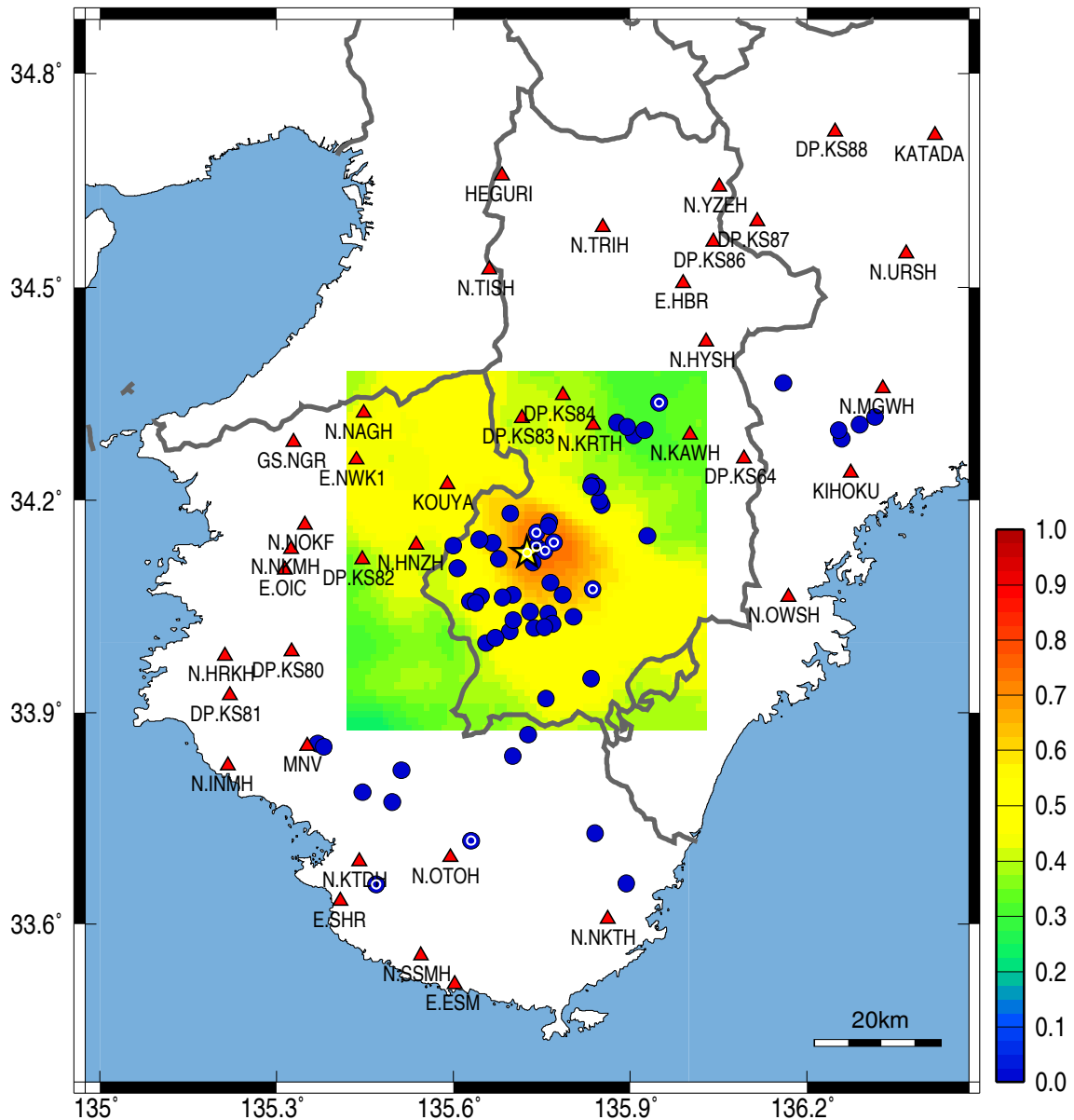


Fig. 2 Distribution of the seismic stations (triangles) and landslides (circles). Landslides identified by seismic records are marked with white circles. The shaded colors show the probability of the location of Akatani landslide, obtained from the back-projection analysis. The star shows the surface location of the Akatani landslide.

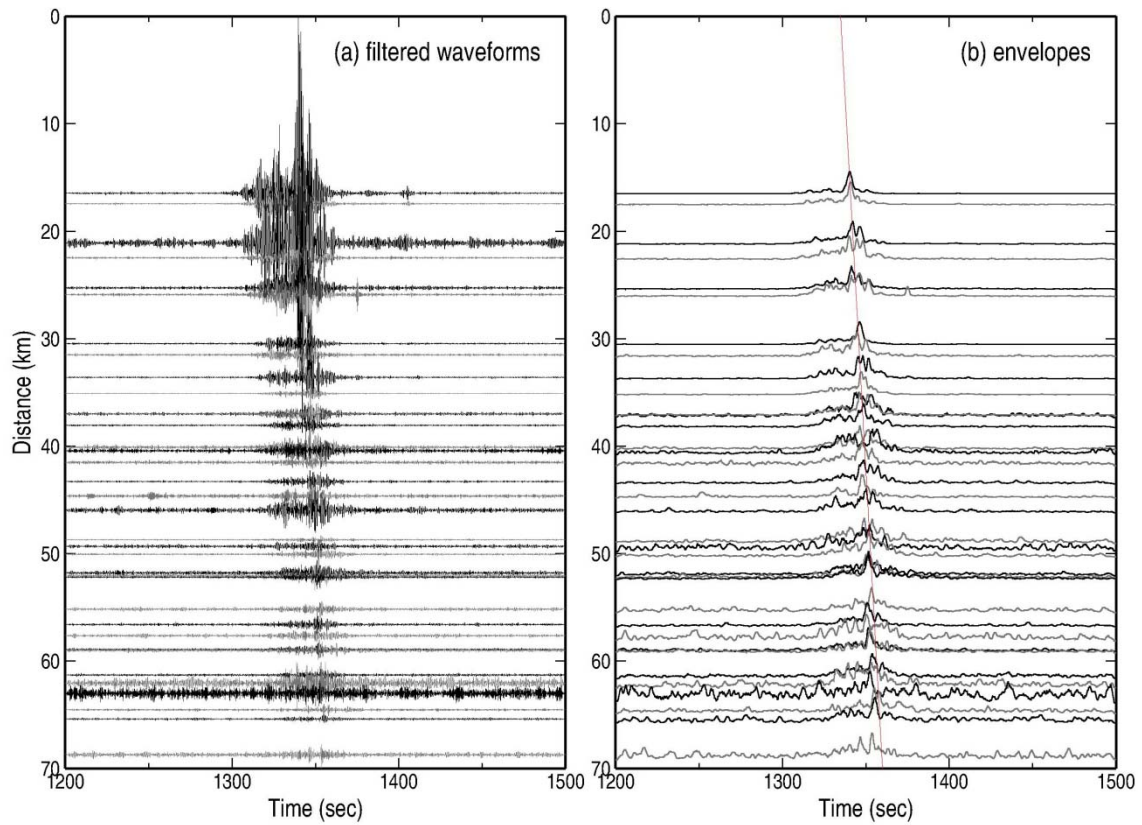


Fig. 3 Seismic records of the Akatani landslide. (a) 1-4Hz band-pass filtered records, (b) processed envelopes for back-projection analysis. Adjacent seismograms are shown alternatingly in black and gray for clarity. The red line shows the predicted arrival time for the location obtained from the back-projection analysis.

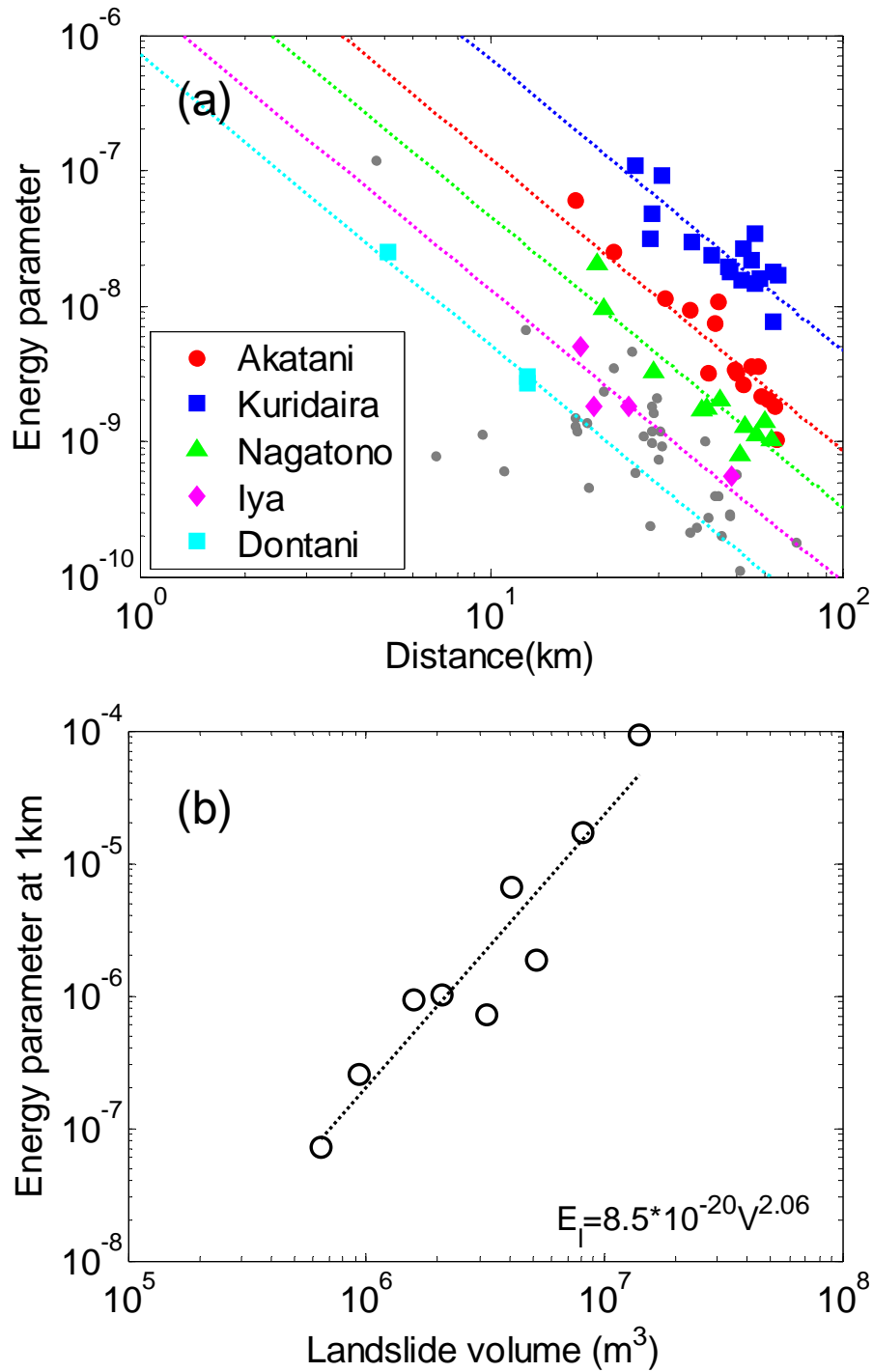


Fig. 4 (a) Energy parameter of different landslides as a function of source-station distance. The lines show regression function for each event. (b) Relationship between volume of the landslide and the energy parameter for a distance 1 km from the source. The line and equation in the figure show the results of a linear regression.

Table 1 List of landslides detected by seismic recordings. Time value shows when the largest high-frequency energy was released. The first 4 digits of the ID show the date of the event. Duration is the average time length of the landslide signal of the high-frequency waveforms. 09031112, 09031114, 09032307, and 09032311 may be subevents of the previous landslide.

ID	Time (UTC)	Back Projection		Surface Location		Error (km)	Landslide Name	Vol. (10^6 m^3)	Duration (s)	β_i
		Lon.	Lat.	Lon.	Lat.					
09030946	9:46:07	135.723	34.169	135.741	34.134	4.2	E.Akatani-1	2.1	30	-5.99
09031112	11:12:29	135.778	34.138	135.741	34.134	4.9	E.Akatani-2	(2.1)	30	-6.06
09031114	11:14:30	135.908	34.108	135.741	34.134	15.6	E.Akatani-3	(2.1)	50	N/A
09031713	17:13:42	135.795	34.086	135.780	34.128	4.9	Uguhara	1.6	40	-6.03
09031758	17:58:11	135.721	34.154						30	-6.10
09031805	18:05:41	135.841	34.163						50	-5.82
09032154	21:54:04	135.580	33.748	135.630	33.718	5.7	Iya	5.2	30	-5.73
09032206	22:06:46	135.801	34.174	135.741	34.154	6.0	Ohto-Shimizu	0.9	30	-6.60
09032306	23:06:13	135.836	34.088	135.836	34.075	1.4	Kuridaira-1	13.6	100	-4.03
09032307	23:07:20	135.825	34.086	135.836	34.075	1.6	Kuridaira-2	(13.6)	30	N/A
09032311	23:11:44	135.826	34.054	135.836	34.075	2.5	Kuridaira-3	(13.6)	20	-6.08
09040002	0:02:13	135.449	33.671	135.469	33.656	2.5	Dontani	3.2	30	-6.14
09040006	0:06:04	135.915	34.284						20	N/A
09040140	1:40:00	135.649	34.126						40	-6.16
09040145	1:45:54	135.745	34.130	135.754	34.129	0.8	Nagatono	4.1	60	-5.19
09040558	5:58:06	136.380	34.370						50	-5.63
09040722	7:22:15	135.715	34.133	135.725	34.126	1.2	Akatani	8.2	70	-4.77
09040825	8:25:39	135.959	34.348	135.949	34.338	1.4	Ohtaki	0.7	50	-7.14